New Insights into the Role of the Synthesis Procedure on the Performance of Co- Based Catalysts for Ethanol Steam Reforming

Ilenia Rossetti[a], Barbara Bonelli[b], Gianguido Ramis[c], Elnaz Bahadori[a], Roberto Nasi[b], Antonio Aronne[d], Serena Esposito[e*]

[a]Dip. Chimica, Università degli Studi di Milano, INSTM Unit Milano-Università and CNR-ISTM, via C. Golgi, 19, I-20133 Milano, Italy.

[b]Dipartimento di Scienza Applicata e Tecnologia, Politecnico di Torino, INSTM Unit of Torino-Politecnico, Corso Duca degli Abruzzi 24, I-10129 Torino, Italy.

[c]Dip. di Ingegneria Civile, Chimica e Ambientale, Università degli Studi di Genova and INSTM Unit Genova, via all'Opera Pia 15A, Genova, Italy.

[d]Dipartimento di Ingegneria Chimica, dei Materiali e della Produzione Industriale, Università degli Studi di Napoli Federico II, Piazzele Tecchio, 80 – I-80125 Napoli (Italy)

[e]Dipartimento di Ingegneria Civile e Meccanica and INSTM Unit- Università di Cassino, Via G. Di Biasio 43, 03043 Cassino (Fr), Italy.

* Dott.ssa Serena Esposito
Dipartimento di Ingegneria Civile e Meccanica
Università di Cassino
Via G. Di Biasio 43, 03043 Cassino (Fr), Italy
Tel: +39 0776 2993697
Fax: +39 0776 2993711
E-mail: s.esposito@unicas.it

Abstract

Co/SiO$_2$ catalysts with two Co contents of 10 and 30 mol % were prepared and used in ethanol steam reforming. With the aim of tailoring the materials features by varying the synthesis parameters, two different sol-gel procedures were designed, namely a modified hydrolytic alkoxide sol-gel synthesis and a (non-ionic) surfactant assisted one.

Effect of the synthesis procedure on the physico-chemical properties of the prepared catalysts is in the focus of the present investigation. The obtained Co/SiO$_2$ catalysts were characterized by means of X-rays powder diffraction (XRPD); Diffuse Reflectance UV-Vis spectroscopy; N$_2$ adsorption/desorption isotherms at -196°C; field emission scanning electron microscopy equipped with Energy Dispersive X-ray probe (FESEM-EDX); temperature-programmed reduction (TPR) and CO adsorption at nominal -196C° as followed by IR spectroscopy.

The oxidation state of Co species within the SiO$_2$ matrix was affected by the synthesis method. In particular, the non-ionic surfactant, acting both as pores template and as chelating agent of Co ions during the synthesis, prevented the formation of Co$_3$O$_4$ phase, leading to a higher dispersion, and higher temperature reducibility of Co species with respect to samples with same Co content synthesized without surfactant.

The fine balance between Co dispersion and reducibility was the fundamental parameter governing the activity of the Co/SiO$_2$ catalysts in terms of H$_2$ production; CO/CO$_2$ ratio and C balance during ethanol steam reforming.

1. Introduction

As far as transition metals-based systems are concerned, Co-containing nanomaterials have always attracted great scientific interest due to their performance in a wide range of applications. Indeed, they are used as catalysts in many reactions; as electrochromic devices; as magnetic materials and as molecular sieve membranes [1-7]. Recently, Co has emerged as the most versatile non-noble metal for the development of H_2- and O_2-evolving catalysts in the water splitting reaction [8-15].

The steam reforming of biofuels, such as ethanol (EtOH), is currently a "hot" research topic, where Co has always played a primarily role as an active (non-precious) metal catalyst for C-C bond cleavage [7, 16-19].

EtOH steam reforming (ESR) implies a complex set of possible reactions, the most relevant one being represented by eq. (1):

$$CH_3CH_2OH+3H_2O \rightarrow 2CO_2 +6H_2 \qquad (1)$$

which may be seen as the sum of the syngas production reaction (eq. (2)) and the water gas shift (WGS) reaction (eq. (3)):

$$CH_3CH_2OH+H_2O \rightarrow 2CO+4H_2 \qquad (2)$$

$$CO+H_2O \rightleftharpoons CO_2 +H_2 \qquad (3)$$
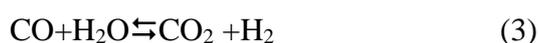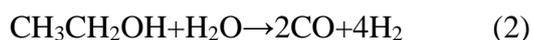
A suitable ESR catalyst should respond to severe requirements, in order to overcome undesired parasitic reactions, during which EtOH may be dehydrogenated to acetaldehyde (that can be further reformed), but also undergo dehydration to ethylene: the latter moiety can then polymerize, leading to formation of carbonaceous deposits on the catalyst. Furthermore, depending on the operating conditions, other parasitic reactions may induce coke formation, like CO disproportionation through the Boudouard reaction (occurring at mild temperature) or decomposition of hydrocarbons (occurring at high temperature [20-22]),

Selection of a proper support is crucial, in that the support strongly affects Co dispersion, particle size and reducibility and, finally, catalytic activity. Furthermore, the support surface acidity

affects catalytic activity towards EtOH dehydration to ethylene (strictly related to coke formation) [22].

SiO$_2$ supported Co is one of the most versatile catalysts, because SiO$_2$ has excellent chemical and thermal stability, fair accessibility and porosity, and because organic groups can be anchored at the surface providing stable catalytic centers [18, 19, 23, 24].

Co redox chemistry, *i.e.* Co species forming and interacting with SiO$_2$, represents a crucial issue in the design of a catalyst with high ESR performance. High valence Co species, *i.e.* those occurring in the cubic spinel Co$_3$O$_4$, are considered the precursor of the metallic catalytic species (Co^0), in virtue of their low temperature reducibility. A.J. Vizcaíno *et al.* [25] studied SBA-15 supported Co catalysts modified by addition of Mg and Ca. Notwithstanding a higher Co dispersion in the alkali-earth promoted samples (where a negligible fraction of Co$_3$O$_4$ crystalline phase formed and strongest metal–support interaction occurred) showed a lower ESR performance from the point of view of both EtOH conversion and selectivity to H$_2$. This behavior was ascribed to the high temperature needed for Co species reduction in alkali-earth promoted catalysts with respect to bare Co/SBA-15.

On the other hand, segregation of Co$_3$O$_4$ is symptomatic of a low dispersion of Co species, which in turns is detrimental for catalytic activity [18-19]. Some of us have shown [18] that aabsence of Co segregation, even if combined with the presence of Co phases reducible at high temperature, is the key factor in the activity of ESR catalysts.

Though several works concern the application of Co/SiO$_2$ materials as steam reforming catalysts, there is still lack of fundamental studies on how "to play" with Co redox chemistry, in order to comply with the need of a fine balance among Co reducibility, dispersion and reactivity.

With respect to other preparation methods, the sol-gel procedure has the advantage of allowing a proper modulation of catalyst surface properties through an accurate control of synthesis conditions [26-30].

In this work two different procedures were adopted, namely a modified hydrolytic alkoxide sol-gel route and a non-ionic surfactant assisted sol-gel route.

SiO_2 supported Co catalysts (with either 10 or 30 mol % Co content) were prepared with the purpose of investigating how the preparation method may drive the formation of specific Co phase(s), finally tailoring the catalytic features.

All the catalysts were characterized by X-ray powder diffraction (XRPD); N_2 adsorption/desorption isotherms at -196°C; field emission scanning electron microscopy equipped with Energy Dispersive X-ray probe (FESEM-EDX); temperature-programmed reduction (TPR); Diffuse Reflectance (DR) UV-Vis spectroscopy and CO adsorption at nominal -196 C° as followed by IR spectroscopy.

Catalytic activity tests were performed in a homemade micro-pilot plant for ESR under different process conditions. Since coke formation during ESR is an issue, the catalysts physico-chemical properties were finely tuned, in order to improve catalysts performance at low temperature, particularly severe for coke deposition.

2. Experimental

2.1 *Materials synthesis*

Cobalt nitrate hexahydrate ($Co(NO_3)_2 \cdot 6H_2O$, Acros Organics), Tetraethoxysilane (TEOS, $Si(OC_2H_5)_4$ 99 %, Aldrich) and polyethylene glycol hexadecyl ether ($C_{16}H_{33}(OCH_2CH_2)_{10}OH$, Brij® C10, Sigma-Aldrich), were used as starting reagents. Two sets of samples with either 10 or 30 mol % Co content were prepared: the former was obtained without any surfactant (samples hereafter referred to as: a-10Co and a-30Co) and the latter with addition of Brij® C10 (samples hereafter referred to as: b-10Co and b-30Co).

During the synthesis of a-10Co and a-30Co samples, TEOS was hydrolysed at 50°C without any alcoholic solvent, by using concentrate HNO_3 (70%, , ≥99.999% trace metals basis) as catalyst, in the following molar ratio TEOS : H_2O : HNO_3 = 1 : 4 : 0.01. The absence of an alcoholic solvent

sets the system in the "immiscibility" state. However, as TEOS hydrolysis takes place with both water consumption and alcohol production, the system moves towards the miscibility region. The clear sol obtained after 1 hour stirring was cooled to room temperature (r.t.) and a suitable amount of $Co(NO_3)_2 \cdot 6H_2O$ was slowly added.

Only during the preparation of b-10Co and b-30Co samples, the non-ionic surfactant was added to the prepared solution (15 g per 100 mL solution). The gel formed at r.t. after 24 h in case of a- samples, and in 48 h with b- samples. All the gelled systems were kept for 3 days at r.t. before drying and then were fully dried in air at 110°C in an electric oven for 12 h.

The dried a-10Co and a-30Co samples were heat treated ($10 \, °C \cdot min^{-1}$) at 400 °C to eliminate all the organic residue and at 850 °C for 1h (a-10Co400 and a-10Co850).

The dried b-10Co and b-30Co samples were heat treated ($10°C \cdot min^{-1}$) at 500°C for 2 hours in order to remove the non-ionic surfactant (b-10Co500, b-30Co500) and 850 °C for 1h (b-10Co500 and b-10Co850).

2.2 *Materials characterization*

X-ray Powder Diffraction (XRPD) patterns were obtained on a X'Pert Phillips diffractometer operating with Cu K_α radiation (1.541874 Å) with a step width of 0.02° 2θ and 2.00 s time per step. Average crystallite size was determined from XRPD patterns by means of the Debye–Scherrer formula ($D = 0.9\lambda/bcos\theta$, where λ is the wavelength of the Cu K_α radiation, b is the peak full width at half maximum in radians, 0.9 is the shape factor for spherical particles and θ is the diffraction angle).

Field emission scanning electron microscopy (FESEM) pictures were taken on a ZEISS Supra 40 FESEM instrument. The same is equipped with an EDX (Energy Dispersive X-ray) probe that was used here to determine (semi-quantitatively) chemical composition of the samples on 10 – 50 nm diameter spots (for each samples, 5 spots were considered and the corresponding average values were calculated).

N$_2$ adsorption/desorption isotherms at -196°C were measured on samples previously outgassed at 300 °C to remove water and other atmospheric contaminants (Quantachrome Autosorb 1 apparatus). Samples specific surface area (SSA) was calculated according to the BET (Brunauer–Emmett–Teller) method; total pore volume was determined from adsorbed amounts at *P/P$_0$* = 0.98 and micropore volume was calculated according to the *t*-plot method. Samples pore size distribution (PSD) was calculated by applying the Non Local-Density Functional Theory (NL-DFT) method to isotherm adsorption branch, by using a N$_2$-silica kernel. The obtained values are reported in Table 1. Diffuse reflectance (DR) UV-Vis spectra of powders were measured on a Cary 5000 UV-vis-NIR spectrophotometer (Varian instruments), equipped with an integration sphere; the so obtained DR-UV-Vis spectra are reported as Kubelka–Munk function (*F*(*R*)).

Temperature Programmed Reduction (TPR) measurements were carried out in a laboratory flow apparatus, using a 5 vol. % H$_2$/Ar (Q = 20 cm^3 min^{-1}) with heating rate of 10 $^\circ$C min^{-1} up to 800°C. In a typical TPR experiment, *ca.* 100 mg sample was loaded in a quartz down-flow cell with a K thermocouple in close contact with the sample.

For IR measurements, samples were shaped into thin, self-supporting wafers (*ca.* 15 mg cm^{-2}) and pre-treated in a standard vacuum frame (residual pressure below 10^{-3} mbar): the samples were either outgassed at 500°C under vacuum or reduced under a H$_{2(g)}$ equilibrium pressure of *ca.* 30.0 mbar. The b-30Co500 was reduced at 500°C, whereas the a-30Co400 sample was reduced at 400 °C, since at 500°C a dramatic loss of transparency occurred, likely due to a massive reduction to Co^0 particles.

As a consistent loss of transparency occurred after reduction in H$_{2(g)}$ at 500°C (likely due to formation of Co^0 particles), only IR spectra concerning samples either outgassed or reduced at 400°C will be reported. IR spectra were recorded of the samples both as such and after dosing CO (equilibrium partial pressure in the 0.001 – 30.0 mbar range) at nominal -196°C, in a homemade IR cell, which allows us to carry out thermal treatments and dose gases. Fourier transform (FT) IR

spectra were recorded at 2 cm^{-1} resolution on a Bruker Equinox 55 spectrophotometer equipped with a MCT (mercury cadmium telluride) cryodetector.

2.3 *ESR catalytic tests*

Catalytic activity tests were carried out by means of a continuous micro-pilot plant. It includes an Incoloy 800 downflow reactor (i.d. 0.9 cm; length 40 cm), heated by an electric oven. The reactor temperature was controlled by an Eurotherm 3204 TIC temperature controller. The catalysts were pressed, ground and sieved into 0.15–0.25 mm particles, then *ca.* 0.5 g catalyst was loaded into the reactor after dilution 1:3 (v/v) with SiC of the same particle size. Catalyst activation was accomplished by feeding 50 cm^3 min^{-1} of a 20 vol% H$_2$/N$_2$ gas mixture, while heating by 10°C min^{-1} up to 500°C or 800°C for 1 h. The pressure drop across the reactor was negligible (few mbar) and reproducible for every test.

0.017 cm^3 min^{-1} of a 3:1 (mol/mol) H$_2$O:CH$_3$CH$_2$OH liquid feed were continuously supplied to the reactor by means of a Hitachi, mod. L7100, HPLC pump. The reactor was fed with 56 cm^3 min^{-1} of N$_2$ (internal standard) and 174 cm^3 min^{-1} of He. Activity runs were carried out at atmospheric pressure, GHSV = 2500 h^{-1} (referred to the ethanol + water gaseous mixture) at 625 and 750°C. The products were analyzed by a gas chromatograph (Agilent, mod. 7980) equipped with two columns connected in series (MS and Poraplot Q) with a thermal conductivity detector (TCD), properly calibrated for the detection of ethanol, acetaldehyde, acetic acid, acetone, water, ethylene, CO, CO$_2$, H$_2$. Material balance on C-containing products was checked to quantify coke deposition (C-balance). Repeated analyses of the effluent gas were carried out every hour and the whole duration of every test at each temperature was ca. 8 h. Results are reported as mean over 4-8 h-on-stream. The raw data, expressed as mol/min of each species outflowing from the reactor, have been elaborated as reported in [22].

Before testing, all the obtained catalysts were activated by *in situ* reduction at 800°C.

3. Results and discussion

3.1 About the adopted sol-gel synthesis procedure

During the sol-gel synthesis of samples without surfactant, TEOS first underwent acid catalyzed hydrolysis in aqueous environment according to a modified sol–gel method previously reported [1,18]. In a second step, $Co(NO_3)_2$ $6H_2O$ was added to partially hydrolyzed TEOS mixture, giving rise to a pinkish colored solution, as typical of the occurrence of $[Co(H_2O)6]^{2+}$ aquo-ions. In such conditions, gelation is the result of polycondensation reactions involving partially hydrolyzed $Si(OR)_x(OH)_y$ oligomers. Therefore, all wet gels will be formed by a siloxanes network, in which Co species are physically "trapped" [23].

In the surfactant-assisted sol-gel synthesis, we have explored an unconventional use of the non-ionic surfactant in the synthesis of Co/SiO_2 catalysts. Usually, micelle-templated mesostructures are obtained by dropping the SiO_2 precursor in an aqueous solution of the surfactant, followed by hydrothermal treatment at about 100 °C for several hours [31-33]. Such approach exploits the aggregation of non-ionic surfactant molecules as a structure-directing principle for the generation of ordered mesoporous silica structure [34]. These mesoporous silicas are then impregnated with cobalt salt solution to obtain catalysts precursors. However, this method has a poor control on particles distribution on the support and yields a weak binding between metal and support. Weakley attached metal particles to the support tend to aggregate forming big particles which catalyzed coke formation. Moreover, introduction of a high Co content in mesoporous SiO_2 by a one-pot procedure is still challenging being the cobalt amount in the final sample pH dependent [31-32]. We adopted such procedure as a challenging route for the immobilization of high Co contents in the SiO_2 matrix.

On the one hand, a high metal loading is usually required for non-noble transition metals based ESR catalysts, as low Co (and Ni) amounts usually lead to poorly active ESR catalysts. On the other hand, such a high metal loading would likely lead to formation of large metal particles, which may

be responsible of coking. Indeed, large Co (and Ni) particles are more prone to the formation of multi-walled carbon nanotubes: the latter sometimes induce detachment of the active phase from catalyst surface, with consequent reactor blockage by fouling and clogging [18, 19, 35]. Thus, the here adopted sol-gel synthesis procedure for catalyst preparation aims at obtaining a suitable dispersion of the active phase in the catalyst matrix, in order to achieve sufficiently active and stable catalysts.

In the present work, Brij® C10 was added to the solution containing partially hydrolyzed $Si(OR)x(OH)_y$ and $[Co(H_2O)6]^{2+}$ aquo-ions, acting as porosity template yielding to a transparent pinkish gel containing encapsulated surfactant rather than a ordered mesostructured SiO_2. Brij® C10 resulted to be effective as an oxygen-rich complexing agent of the metallic species preventing the formation high-valence Co oxide clusters (*i.e.* Co_3O_4) as evidenced by the physico-chemical characterization reported below.

3.2 *Catalysts structural and textural characterization*

The chemistry of Co is characterized by the two oxides CoO and Co_3O_4: the latter is the most stable phase at r.t. and is reduced to (stoichiometric) CoO above 950°C. Co_3O_4 can be depicted as a $Co^{2+} Co_2^{3+}O_4$ mixed valence oxide with a cubic spinel structure, where Co^{2+} and Co^{3+} ions occupy one-eighth of tetrahedral (Td) sites and one-half of octahedral (Od) sites, respectively. Formation of Co_3O_4 inside SiO_2 matrices is also strictly affected by the preparation method [19, 23, 24].

The XRPD patterns of the a-10Co400 and b-10Co500 samples (not reported for sake of brevity) merely displayed a broad signal at $2\theta \cong 22°$, typical of amorphous SiO_2/silicates. The high homogeneity of Co species, as obtained through the sol-gel preparation, limits Co_3O_4 formation as one would expect from thermal decomposition of the Co precursor (*i.e.* $Co(NO_3)_2 \cdot 6H_2O$, T_{dec} = 242°C). Conversely, the main peaks of Co_3O_4 are usually present in XRD patterns of Co-impregnated porous SiO_2 [19, 24].

Factors affecting the Co_2SiO_4 formation, *i.e.* whether it results from the synthesis procedure or is promoted by the reduction treatment, are largely debated, since the silicate could be responsible of too high (thus impractical) reduction temperature of the catalysts. [6, 25]. Formation of Co_2SiO_4 was previously explored by some us through a high temperature flame pyrolysis synthesis, as a tool to achieve high Co dispersion in Co/SiO_2 catalysts, with improvement of activity and stability with respect to samples obtained by impregnation, a procedure that achieved lower Co dispersion [18].

In order to solve this issue, the present samples were treated at 850°C, a temperature selected on the basis of thermal analysis curves (not reported) showing an exothermic peak at 800°C, likely due to some crystallization phenomenon: formation of the crystalline Co_2SiO_4 phase (JCPDS card 15-0865) was indeed observed with both a-10Co850 and b-10Co850 (Fig. 1). Occurrence of the silicate was indicative of a strong interaction between Co^{2+} ions and the siloxane matrix.

Increase of the Co content up to 30 mol% favoured crystallization of Co_3O_4 (JCPDS card 42-1467) in the a-30Co400 sample (Fig 2A). It is worth to mention that the average size of Co_3O_4 crystallites was in the nanometric scale (about 15 nm), suggesting a high Co dispersion within the SiO_2 matrix, as requested for catalytic applications.

FESEM pictures in Fig. 3 show indeed that the samples have a markedly different morphology, in that the a-30Co400 sample (Figs. 3a and 3b) shows the occurrence of nearly spherical particles with a high tendency to aggregation: the EDX probe showed a high Co concentration (ca. 35 mol %) on such particles and a lower one in other regions of the sample, indicating a poor Co homogeneity. With the b-30Co500 sample (Fig. 3c) instead, such particles were not observed and the average Co content, as calculated from 5 EDX measurements on 5 different spots was ca. 29 mol %, i.e. very close to the nominal composition.

Moreover, the non-ionic surfactant assisted synthesis led to a completely amorphous sample after thermal treatment up to 500°C, as clearly evidenced by the XPRD pattern of the b-30Co500 sample (Fig 2A). Absence of the Co_3O_4 phase is indicative of a much higher dispersion of Co species in the sample, likely achieved by addition of the non-ionic surfactant that, through O atoms

11

of its ethoxy groups, is able to chelate metal ions. Moreover, since the Co precursor is a salt of Co^{2+}, formation of the Co_3O_4 mixed oxide occurs by oxidation of a fraction of Co^{2+} species to Co^{3+} species. Actually, the surfactant itself (i.e. a polyethylene glycol hexadecyl ether) might create a reducing environment, inhibiting oxidation of all the Co^{2+} species.

At 850°C, crystallization of the Co_2SiO_4 phase (JCPDS card 15-0865) started to occur with both samples, being the only crystalline phase with the b-10Co850 sample (Fig. 2B). With the a-30Co850 sample, the presence of both Co_2SiO_4 and Co_3O_4 phases indicates that a fraction of Co^{2+} species, likely embedded within the siloxane matrix, cannot transform into Co_3O_4 during treatment at 400°C.

The DR UV-VIS spectra of the samples heated at low temperatures, namely b-10Co500 and a-10Co400, are shown in Fig. 4A: the triplet of bands at 525, 585 and 645 nm is typical of the $^4A_2$ (F) $\rightarrow$ $^4T_1$ (P) transition of Td Co^{2+} ions. In samples treated low temperatures, Co^{2+} ions likely occurs as [$Co(OH)_4$]- or [CoO_4]- species coordinated by the silica matrix [23].

Thermal treatment at 400°C leads to the formation of cobalt mixed valence oxide [$Co^{3+}_2Co^{2+}O_4^{2-}$] with Td Co^{2+} and Od Co^{3+} ions in the a-30Co400 sample (Fig 4B). This idea is supported by absorption bands at about 400 and 700 nm as well as by the black colour of the sample [1, 18]. Conversely, thermal treatment at 500°C possibly induces, in the b-30Co500 sample, a partial oxidation of Co^{2+} to Co^{3+} in agreement with the occurrence of a not well-resolved peak at 350 nm (Fig. 4B). Nevertheless, the bands at 520, 591 and 640 nm resemble those due to the $^4A_2$ (F) $\rightarrow$ $^4T_1$ (P) transition of Td Co^{2+} species. Therefore, the surfactant deeply affects the chemical interactions between Co ions and the silica matrix, as well as Co dispersion, finally avoiding the formation of Co_3O_4 even at 30 mol% Co content.

The N_2 adsorption-desorption isotherms of thermally treated samples are reported in Fig. 5A and 5B. The a-10Co400 and b-10Co500 samples (Fig. 5A) show type I isotherms, as typical of microporous materials where the slight deviation from the ideal Langmuir shape is ascribable to the presence of some mesoporosity, as confirmed by the corresponding PSDs curves (Fig. 6A and 6B).

The b-10Co500 isotherm shows a plateau at higher values of partial pressure ($P/P^0 > 0.2$) with respect to that of the a-10Co40 isotherms (plateau at $P/P^0 > 0.1$), evidence of a lower fraction of micropores, as shown by micropore area values in Table 1. A higher amount of adsorbed N_2 on the b-10Co500 sample, hence an increasing total pore volume (Table 1), denotes that the surfactant-assisted synthesis implies interaction between silica oligomers and hydrophilic part of the surfactant molecules. Göltner *et al.* [36-37] reviewed the formation mechanisms and the final pore structures of porous silicas obtained by using non-ionic templates, emphasizing how the choice of head group in the supramolecular template is a tool to tailor the wall structure in mesoporous materials. The head groups of the non-ionic surfactant used here are highly soluble in the SiO_2 walls resulting in an intimate interlinking with the inorganic matrix during gelation. Therefore, a significant degree of microporosity can be obtained. These observations are confirmed by the values of surface area, total pore volume and micropore volume reported in Table 1.

On the other hand, the samples with 30 mol% Co show type IV isotherms, as typical of mesoporous materials, with large adsorption volumes at $P/P^0 > 0.4$ and hysteresis loops (Fig 5B). The dependence of surface area on the Co content is consistent with previous results [23], in that the incorporation of Co^{2+} species reduces microporosity, since it affects the dehydroxylation mechanism.

Unlike the samples with 10 mol% Co, both a-30Co400 and b-30Co500 samples possess comparable values of total pore volume and have negligible micropore volumes. The data in Table 1 point out the effect, with sol-gel prepared Co/SiO_2 materials, of surfactant addition, causing a noteworthy increase of the surface area as well as a change in the PSDs.

The relative abundance of both micropores and mesopores and the effectiveness of the synthesis procedure on the modification of the textural properties can be better appreciated in the corresponding PSDs (Figures 6A and 6B). While the a-10Co400 sample appears entirely microporous, the b-10Co500 sample presents a fraction of pores in the (small) mesopores range between 20-40 Å. The two samples with 30 mol% Co show mainly mesopores with a negligible

amount of micropores. Nevertheless, the non-ionic surfactant in the b-30Co500 sample causes the shift of the whole PSD curve toward larger pore size.

In order to gain a greater insight into the Co/SiO_2 interaction as function of the synthesis procedure, the samples reducibility was studied by means of TPR. The curve fit analysis of TPR profiles (not reported) allowed obtaining the amount of H_2 consumed corresponding to each reduction peak, as well as an estimation of the different amounts of Co species occurring as: (i) Co_3O_4 phase; (ii) amorphous silicate (reduced at 700–800°C) and (iii) not reducible Co species (Table 2).

The a-10Co400 sample shows a very weak TPR signal, with reduction peaks at 305 and 798°C: the former could be ascribed to reduction of isolated Co^{2+}/Co^{3+} species and the latter to reduction of Co^{2+} ions strongly interacting with (or bonded to) the siloxane framework [28]. The species reducible at higher temperatures can be regarded as belonging to an amorphous silicate, showing similar redox properties, although the Co_2SiO_4 crystalline phase forms only at higher temperature, as observed by XRPD (2B). With the a-10Co400 sample, most of the Co species is strongly interacting with the SiO_2 matrix, resulting not accessible for reduction. With the b-10Co500 sample, the chelating action of the surfactant substantially increases the fraction of reducible dispersed Co species, whereas the non-reducible remaining fraction is likely occurring as crystalline Co_2SiO_4.

TPR curves of the samples with 30 mol% Co content show a pair of more intense reduction peaks in the 300–400°C range, followed by other signals in the 700–800°C range. The peaks in the 300–400°C range are generally ascribed to the two-steps reduction of supported Co_3O_4, whereas pure Co_3O_4 gives only one TPR signal [38].

According to TPR results, the surfactant assisted sol-gel synthesis prevents Co agglomeration leading to discrete domains, finely dispersed within the silica matrix, reducible at higher temperature with respect segregated Co_3O_4 phase. Nevertheless, the fraction of reducible Co species appears comparable to that occurring with the a-30Co400 sample (Table 2).

3.3 CO adsorption at nominal -196°C as followed by IR spectroscopy

IR spectroscopic characterization was performed on the two samples with 30 mol% Co content, as the catalytic tests showed they had better performance (*vide infra*).

As a probe molecule, CO is able to interact with both hydroxyls groups (usually found at the surface of oxides) and with Lewis sites, giving rise to characteristics IR bands in the CO stretching range (2200-1700 cm^{-1}) that allow to infer both oxidation state and coordination of surface metal ions [39]. Difference IR spectra are hereafter reported, as obtained by subtraction of IR spectra of the bare samples (not reported).

CO dosage on the two samples outgassed at 500°C leads to different IR spectroscopic features, as shown by the corresponding IR spectra reported in Figs. 7A and 7B. In order to allow comparison, all the IR spectra hereafter reported have been normalized to sample unit thickness.

CO adsorption on the a-30Co400 sample outgassed at 500°C (Fig. 7A) gives rise to the formation of four bands at 2156, 2137, 2125 and 2110 cm^{-1}, respectively. The 2156 cm^{-1} band is assigned to CO molecules interacting with free silanols (SiOH groups originally absorbing at 3740 cm^{-1} in the bare sample), like those occurring at the surface of amorphous SiO_2, whereas the 2139 cm^{-1} band is assigned to a liquid-like phase forming when CO is physisorbed at low temperature porous materials [40].

According to the literature, CO molecules adsorbed on Co^{3+} sites at the surface of Co_3O_4 are characterized by a band at 2195 cm^{-1} (shifting to 2175 cm^{-1} at higher CO equilibrium pressure). Such band was not observed here; the 2125 cm^{-1} band, instead, is likely due to CO molecules interacting with Co^{2+} (or Co^+) ions at the surface of a partially reduced Co_3O_4 phase, as a consequence of the treatment at 500 °C under *vacuum*. The band at 2110 cm^{-1} is likely due to Co^{2+} species, but in a different environment, since CO molecules interacting with Co^{2+}/ Co^+ species at the surface of Co_3O_4 are expected to absorb in the 2145-2120 cm^{-1} range. According to the literature, CO adsorption on CoO phase leads to formation of Co^{2+}-CO species characterized by an IR band at 2136 cm^{-1} (shifting to 2112 cm^{-1} at higher CO equilibrium pressure). Here, the presence

of physisorbed CO could hamper the detection of the 2136 cm^{-1} band due to Co^{2+}-CO species at low CO pressures. When CO is dosed on the b-30Co500 sample outgassed at 500°C (Figure 7B), IR bands are seen at 2173, 2156, 2137, 2110 and 1880 cm^{-1}: those at 2156 and 2137 cm^{-1} have the same nature as those observed with the a-30Co400 sample; the 2173 cm^{-1} band, instead, is typical of CO adsorbed on Co^{2+} species in Co^{2+}/SiO$_2$ systems. Moreover, less intense IR bands are observed with the b-30Co500 sample, likely due to the formation of a Co silicate, favored by the non-ionic surfactant assisted synthesis. Finally, a band at 1880 cm^{-1} (also present in Fig. 7A) is due to CO molecules adsorbed on reduced Co species, as according to the literature [40] multicarbonyls of Co^0 (containing both linear and bridging CO molecules) are usually detected in the 2107-2000 cm^{-1} and 1900-1800 cm^{-1} IR ranges.

Figure 8A and 8B report IR spectra taken after dosing CO on both a-30Co400 and b-30Co500 samples after reduction. With the a-30Co400 sample (Fig. 8A): besides the band due to CO interacting with SiOHs groups, bands are seen at 2110, 2070 and 1880 cm^{-1}. The band at 2110 cm^{-1} was already present after outgassing under vacuum at the same temperature, indicating that the corresponding Co species are stable towards reduction in H$_2$ at 400°C, whereas the bands at 2070 and 1880 cm-1 are assigned to multicabonyls species on Co^0 particles (*vide supra*). Corresponding IR spectra concerning CO adsorption on reduced b-30Co500 sample are reported in Fig. 8B: evidence of the occurrence of some reduced Co species is given by bands at 2061, 2010 and 1880 cm^{-1}, whereas more oxidized Co species (on which adsorbed CO originate bands at 2181 and 2110 cm^{-1}) are stable towards reduction. Again, lower IR spectra intensities are observed with the b-30Co500 sample, likely indicating the formation of a Co silicate where a lesser amount of Co is accessible to the probe. This latter result will be confirmed by the sample catalytic performance discussed in the following paragraph.

3.4 *Catalytic activity towards ESR*

The samples were tested for ESR at variable temperature, ranging from 300°C to 750°C. Satisfactory activity and carbon balance. *i.e.* sufficient resistance to coking, were achieved at relatively high temperature. Hence, the results of testing at 625 and 750°C were reported in Table 3. Full EtOH conversion was achieved at 750°C for every catalyst, whereas at 625°C only for the 30 mol % Co loaded samples. A decrease of the operating temperature to 500°C induced a marked decrease of the EtOH conversion of b-30Co500 catalyst to 28% and nil conversion at 400°C. In both cases, acetaldehyde was the main product, with negligible amounts of both ethylene and methane. Moreover, a decreasing activity pattern was observed during the 8 hours of testing at 500 and 400°C, whereas at higher operating temperature constant products distribution, conversion and C balance patterns were achieved with time-on-stream. Consequently, we focused our attention on the tests at 625 and 750°C, only. The samples containing the lowest amount of Co were much less performing than the ones with 30 mol% metal loading. For instance, the b-10Co500 sample gave a limited conversion even at 625°C (87%, only), producing almost exclusively acetaldehyde. The latter by-product was even present at 750°C in some percentage. Also, some instability in performance even at the highest temperature was observed (see for instance the very high error and unreliable C balance result for this sample at 750°C). C balances higher than 100% have been observed in case of the presence of high amounts of acetaldehyde, whose calibration GC curve was less accurate than for gaseous samples and which is often correlated with some coking phenomena. This can explain the fluctuating C balance at high temperature, i.e. due to some accumulation and removal of coke.

Somehow lower acetaldehyde selectivity was achieved when increasing the Co loading (b-30Co500 sample). For sample a-30Co400, the selectivity to methane decreases as expected with temperature, since at higher temperature methane reforming should be more favoured than at lower values. In the case of both sample b, apparently the selectivity to CH_4 increases with temperature. However, we can notice a parallel conversion of acetaldehyde for both samples when increasing temperature. The decomposition of acetaldehyde goes through the formation of CO and CH_4, which

17

can be further reformed. In this sense, the increase of selectivity of methane with increasing temperature for samples b-10Co500 and b-30Co500 has to be interpreted as an increasing methane formation from the reforming of the acetaldehyde byproduct, which is then only partially converted to reformate.

The activity towards WGS reaction was also monitored by looking at the CO/CO_2 ratio: the lowest this parameter, the highest the activity for CO conversion through WGS. The samples obtained by surfactant assisted synthesis were less active also for this reaction. Indeed, the CO/CO_2 ratio at 625°C was *ca.* 6 with respect to a value of 3.8 for sample a-30Co400.

Finally, by comparing the a-30Co400 and b-30Co500 samples, the latter was systematically less performing. Indeed, at 625°C it led to full conversion, but with main product acetaldehyde, so achieving poor hydrogen productivity. Even when increasing the operating temperature to 750°C the results were worse for b-30Co500 than for a-30Co400, with higher selectivity to methane and higher CO/CO_2 ratio.

The spent samples were characterized by temperature programmed oxidation to quantify any possible coking phenomenon. A very small, low temperature peak was observed for both the a-30Co400 and b-30Co500 samples, corresponding to negligible coking rate. The low oxidation temperature supports the presence of amorphous carbon and excludes a significant presence of graphitic or nanotubular carbon.

All the characterization data support the much higher dispersion of Co in the samples prepared by the surfactant assisted synthesis which were characterized by higher surface area (almost double with respect to a-sample). Moreover, XRPD supported the absence of extended Co phases and the formation of a well dispersed Co_2SiO_4 for b- samples. On one hand, this was the goal in order to avoid coking problems. Indeed, negligible carbon accumulation was observed, which may be rather easily controlled by increasing the steam amount in the feed. On the other hand, too high dispersion, especially in the form of Co silicate, led to unavailable active phase. Indeed, the temperature of reduction of Co was too high for b- samples, with insufficient amount of

activated metal during the reaction. This would impose to raise too much the reduction temperature during activation, which would induce to sintering, so counterbalancing the beneficial effect of Co dispersion during the synthesis. The negative effect of cobalt phase reducible at high temperature was observed by A.J. Vizcaíno et al [25] in Co catalysts supported on SBA-15 modified by Ca and Mg.

Thus, the formation of cobalt silicate may be pursued as a way to improve metal dispersion and to stabilize it, provided that sufficiently reducible silicate forms, as for instance in the case of Co/SiO_2 catalysts prepared by flame pyrolysis [18].

4. Conclusion

The sol-gel synthesis is a powerful tool to design a catalyst with tailored properties; moreover, addition of the non-ionic surfactant in this work affected markedly the redox behavior of Co and the formation of highly dispersed Co phases, finally limiting Co^{2+} oxidation and formation of the spinel phase, Co_3O_4, which instead preferentially forms without the surfactant.

The surfactant assisted synthesis, however, also leads to a more difficult reduction of dispersed Co species, as confirmed by TPR, IR spectroscopy and catalytic tests: unfortunately, this has a detrimental effect of the catalytic activity towards ethanol steam reforming reaction, which counterbalance the fair cobalt dispersion obtained with the surfactant. Catalysts exhibiting too high reduction temperatures are not the best choice for ethanol steam reforming, when the process is carried out at low temperatures, but could instead be interesting for other processes where the metal dispersion is the main requisite of the catalyst.

References

1. Esposito S, Setaro A, Maddalena P, Aronne A, Pernice P, Laracca M (2011) J Sol-Gel Sci. Technol. 60:388–394.

2. Zhang F, Zhang S, Guan N, Schreier, Richter M, Eckelt R, Fricke R (2007) Appl. Catal. B: Environ. 73: 209-219.

3. Li N, Wang X, Derrouiche S, Haller SD, Pfefferle LD (2010) ACS Nano 4 (3):1759-1767.

4. Cui H, Zhang Y, Qui Z, Zhao L, Zhu Y (2010) Appl. Catal. B: Environ. 101: 45-53.

5. Esposito S, Bonelli B, Armandi M, Garrone E, Saracco G (2015) Phys.Chem.Chem.Phys. 17: 10774-10780.

6. Puskas I, Fleisch T H, Full PR, Kaduk JA, Marshall CL, Meyers BL (2006) Appl. Catal. A: General 311: 146-154.

7. Da Silva ALM, den Breejen JP, Mattos LV, Bitter JH, de Jong KP, Noronha FB (2014) J. Catal. 318: 67-74.

8. Artero V, Chavarot-Kerlidou M, Fontecave M (2011) Angew. Chem. Int. Ed. 50: 7238 – 72.

9. Tüysüz H, Hwang YJ, Khan SB, Asiri AM, Yang P (2013) Nano Research 6(1): 47–54.

10. Deng X, Tu H (2014) ACS Catal. 4: 3701-3714.

11. Bonelli B, Armandi M, Hernandez S, Vankova S, Celasco E, Tomatis M, Saracco G, Garrone E (2014) Phys.Chem.Chem.Phys. 16 (15): 7074-7082.

12. Saracco G, Vankova S, Pagliano C, Bonelli B, Garrone E (2014) Phys.Chem.Chem.Phys. 16(13): 6139-6145.

13. Hernández S., Bensaid S, Armandi M, Sacco A, Chiodoni A, Bonelli B, Garrone E, Pirri C, Saracco G (2014) Chem. Eng. J. 238: 17-26.

14. Armandi M, Hernandez S, Vankova S, Zanarini S, Bonelli B, Garrone E (2013) ACS Catal. 3 (6): 1272-1278.

15. Zanarini S, Vankova S, Hernandez S, Ijeri VS, Armandi M, Garrone E, Bonelli B, Onida B, Spinelli P (2012) Chem. Comm.48(46): 5754-5756.

16. Sohn H, Ozkan US (2016) Energ. Fuel. 30:5309-5322.

17. Contreras JL, Salmones J, Colín-Luna JA, Nuño L, Quintana B, Córdova I, Zeifert B, Tapia C, Fuentes GA (2014) Int. J. Hydrogen. Energ 39: 18835-18853.

18. Finocchio E, Rossetti I, Ramis G (2013) Int. J. Hydrogen. Energ. 38: 3213-3225.

19. Rossetti I, Lasso J, Nichele V, Signoretto M, Finocchio E, Ramis G, Di Michele A (2014) Appl. Catal. B: Environ. 150-151: 257-267.

20. Fatsikostas AN, Verykios XE (2004) Journal of Catalysis 225: 439–452.

21. Vicente J, Montenero C, Ereña J, Azkoiti MJ, Bilbao J, Gayubo AG (2014) Int. J. Hydrogen. Energ 39: 12586-12596.

22. Rossetti I, Biffi C, Bianchi CL, Nichele V, Signoretto M, Menegazzo F, Finocchio E, Ramis G, Di Michele A (2012) Appl. Catal. B: Environ. 117– 118: 384– 396.

23. Esposito S, Turco M, Ramis, Bagnasco G, Pernice P, Pagliuca C, Bevilacqua M, Aronne A (2007) Journal of Solid State Chemistry 180: 3341–3350.

24. Khodakov AY, Griboval-Constant A, Bechara R, Villain F (2001) J. Phys. Chem. B 105: 9805-9811.

25. Vizcaíno AJ, Carrero A, Calles JA (2016) Fuel Process. Technol. 146: 99–109.

26. Minieri L, Esposito S., Russo V, Bonelli B, Di Serio M, Silvestri B, Vergara A, Aronne A. (2017) ChemCatChem 9 (8): 1476-1486.

27. Esposito S, Sannino F, Pansini M, Bonelli B, Garrone, E (2013) J. Phys. Chem. C 117 (21): 11203-11210.

28. Danks AE, Hall SR, Schnepp Z (2016) Mater. Horiz. 3:91-112.

29. Sannino F, Ruocco S, Marocco A, Esposito S, Pansini M (2013) Micropor. Mesopor. Mat. 180:178-186.

30. Esposito S, Turco M, Bagnasco G, Cammarano C, Pernice P (2011) Appl. Catal. A: General 403 (1-2): 128-135.

31. Vinu A, Dědeček J, Murugesan V, Harmann M (2002) Chem. Mater. 14: 2433-2435.

32. El Haskouri J, Cabrera S, Gómez-García CJ Guillem C, Latorre J, Beltrán D, Marcos MD, Amorós P (2004) Chem Mater 16: 2805-2813.

33. Hoffmann F, Cornelius M, Morell J, Fröba M (2006) Angew. Int. Ed. 45: 3216-3251.

34. Boissièr C, Larbot A, Bourgaux C, Prouzet E, Bunton CA (2001) Chem Mater 13: 3580-3586.

35. Compagnoni M, Lasso J, Di Michele A, Rossetti I (2016) Catal. Sci. & Technol 6: 6247 - 6257.

36. Göltner-Spickermann C (2002) Curr. Opin. Colloid In. 7: 173-178.

37. Göltner GC, Smarsly B, Berton B, Antonietti M (2001) Chem Mater 13: 1617-1624.

38. Bagnasco G, Cammarano C, Turco M, Esposito S, Aronne a, Pernice P (2008) Thermochim. Acta 471: 51–54.

39. Bonelli B, Onida B, Chen J.D, Galarneau A, Di Renzo F, Fajula F, Garrone E (2004) Micropor. Mesopor. Mat 67(1): 95-106.

40. Hadjivanov KI, Vayssilov GN (2002) Adv. Catal. 47: 307-511.

Table 1. Textural properties of annealed samples as derived from N_2 adsorption isotherms at -196°C.

Sample	Specific Surface Area ($m^2\,g^{-1}$)	Total Pore Volume (cm^3g^{-1})	Micro-pore Volume (cm^3g^{-1})[c]	Pore Diameter (Å)[d]
a-10Co400	396[a] (470)[b]	0.17	0.13	8-20
b-10Co500	794[a] (810)[b]	0.49	0.15	8-50
a-30Co400	392[a]	0.42	0	20-50
b-30Co500	524[a]	0.41	0	20-70

[a] As calculated according to the BET algorithm. [b] As calculated by applying Langmuir equation.

Table 2. Results of TPR measurements.

Sample	Tmax (°C)	H_2 Consumption (mmol g^{-1})	Co distribution %		
			Co_3O_4	Co-silicate	Not reduced
a-10Co400	305; 798	0.14; 0.09	6.50	5.50	88
b-10Co500	310; 800	0.168, 0.46	5.80	29.7	64.5
a-30Co400	322, 410; 707	4.50; 0.52	75.1	11.5	13.4
b-30Co500	319, 398; 800	0.154; 3.54	11.5	71.0	17.5

Table 3. Results of activity tests of ESR for 10Co and 30Co samples.

	b-10Co500	a-30 Co400	b-30 Co500
625 °C			
CO/CO$_2$	6.1 ± 0.3	3.79 ± 0.13	6.6 ± 0.5
C balance (%)	103 ± 4	90.0 ± 1.0	100.3 ± 1.9
Conv. EtOH	0.87 ± 0.04	1.00 ± 0.00	1.00 ± 0.00
H$_2$ productivity (mol/min kg$_{cat}$)	0.61 ±0.05	1.75 ±0.06	0.87 ±0.06

Selectivity to by-products (%).	CH$_4$= 2	CH$_4$ = 5.8	CH$_4$ = 5.3
	CH$_3$CHO = 58.0	CH$_3$CHO = 0.0	CH$_3$CHO = 52
	b-10Co500	**a-30Co400**	**b-30Co500**
750 °C			
CO/CO$_2$	35 ± 2	2.11 ± 0.15	4.7 ± 0.2
C balance (%)	119 ± 14	91 ± 4	90 ± 4
Conv. EtOH	1.00 ± 0.00	1.00 ± 0.00	1.00 ± 0.00
H$_2$ productivity (mol/min kgcat)	1.26 ± 0.18	1.94 ±0.09	1.56 ±0.14
Selectivity to by-products (%).	CH$_4$ = 12.5	CH$_4$ = 5.0	CH$_4$ = 8.6
	CH$_3$CHO = 3.1	CH$_3$CHO = 0.0	CH$_3$CHO = 0.0

Figure Captions

Fig. 1 XRD patterns of samples a-10Co850 and b-10Co850. (o) Co$_2$SiO$_4$ (JCPDS card 15-0865).

Fig. 2 XRD patterns of samples (**A**) a-30Co400 and b-30Co500; (**B**): a-30Co850 and b-30Co850. (o) Co$_2$SiO$_4$ (JCPDS card 15-0865). (*) Co$_3$O$_4$ (JCPDS card 42-1467).

Fig. 3 FE-SEM micrographs of a-30Co400 (a, b) and b-30Co500 (c, d).

Fig. 4 UV-Vis Diffuse reflectance spectra of samples (A) b-10Co500 (dashed line) and a-10Co400 (solid line); (B) b-30Co500 (dashed line) and a-30Co400 (solid line).

Fig. 5 N_2 adsorption-desorption isotherms of the samples (**A**): a-10Co400 (triangles) and b-10Co500 (circle) (**B**): a-30Co400 (triangles) and b-30Co500 (circle). Full symbols: adsorption; empty symbols: desorption.

Fig. 6 Pore size distribution of the samples (**A**): a-10Co400 (triangles) and b-10Co500 (circle) (**B**): a-30Co400 (triangles) and b-30Co500 (circle). Full symbols: adsorption; empty symbols: desorption.

Fig. 7 IR spectra concerning CO adsorption at nominal -196°C on a-30Co400 sample (A) and b-30Co500 sample (B) outgassed at 500°C. In both sections, the CO stretching range is reported (2300-1700 cm^{-1}) of difference IR spectra as obtained by subtraction of the corresponding spectrum of the bare sample (not reported). CO equilibrium pressures in the 0.001 – 30.0 mbar range.

Fig. 8 IR spectra concerning CO adsorption at nominal -196°C on reduced a-30Co400 sample (A) and b-30Co500 sample (B). In both sections, the CO stretching range is reported (2300-1700 cm^{-1}) of difference IR spectra as obtained by subtraction of the corresponding spectrum of the bare sample (not reported). CO equilibrium pressures in the 0.001 – 30.0 mbar range.

Fig. 1

Fig. 2

(a) a-30Co400   100 nm

(b) a-30Co400   20 nm

V 1 = 20.56 nm
H 2 = 19.83 nm
H 4 = 16.89 nm
V 2 = 18.36 nm
H 1 = 53.61 nm
H 3 = 21.30 nm

(c) b-30Co500   100 nm
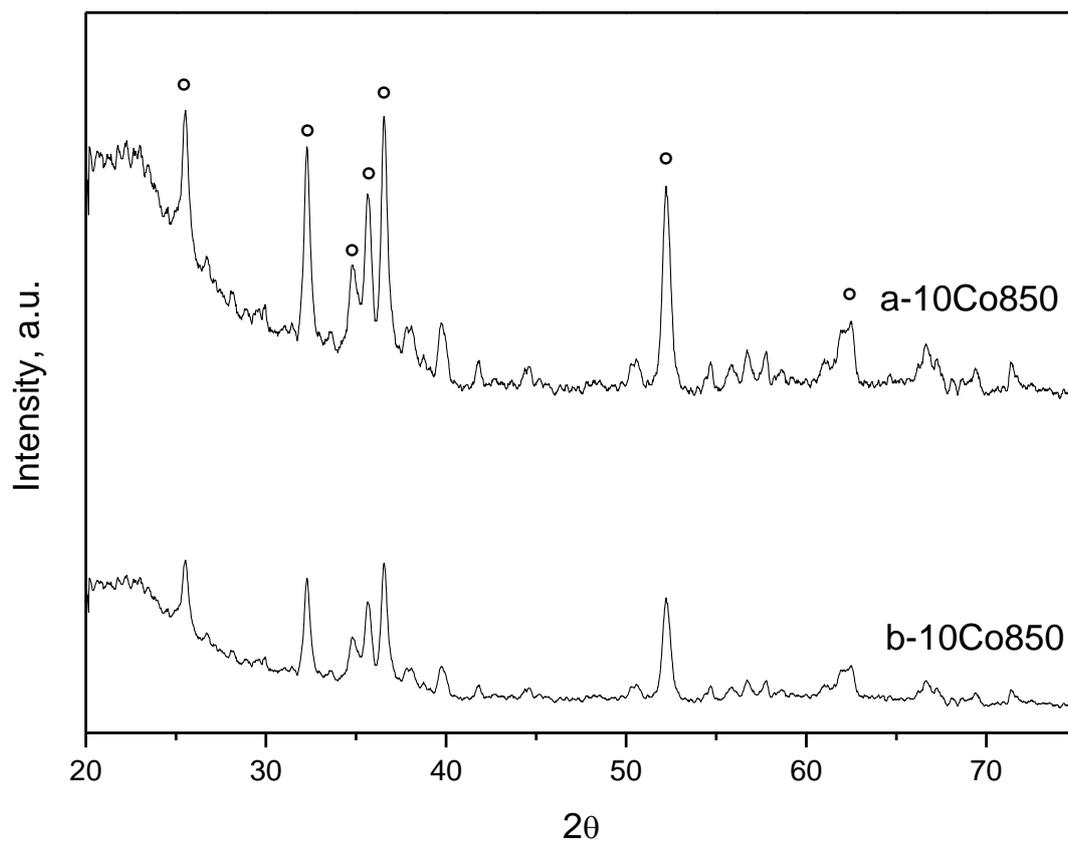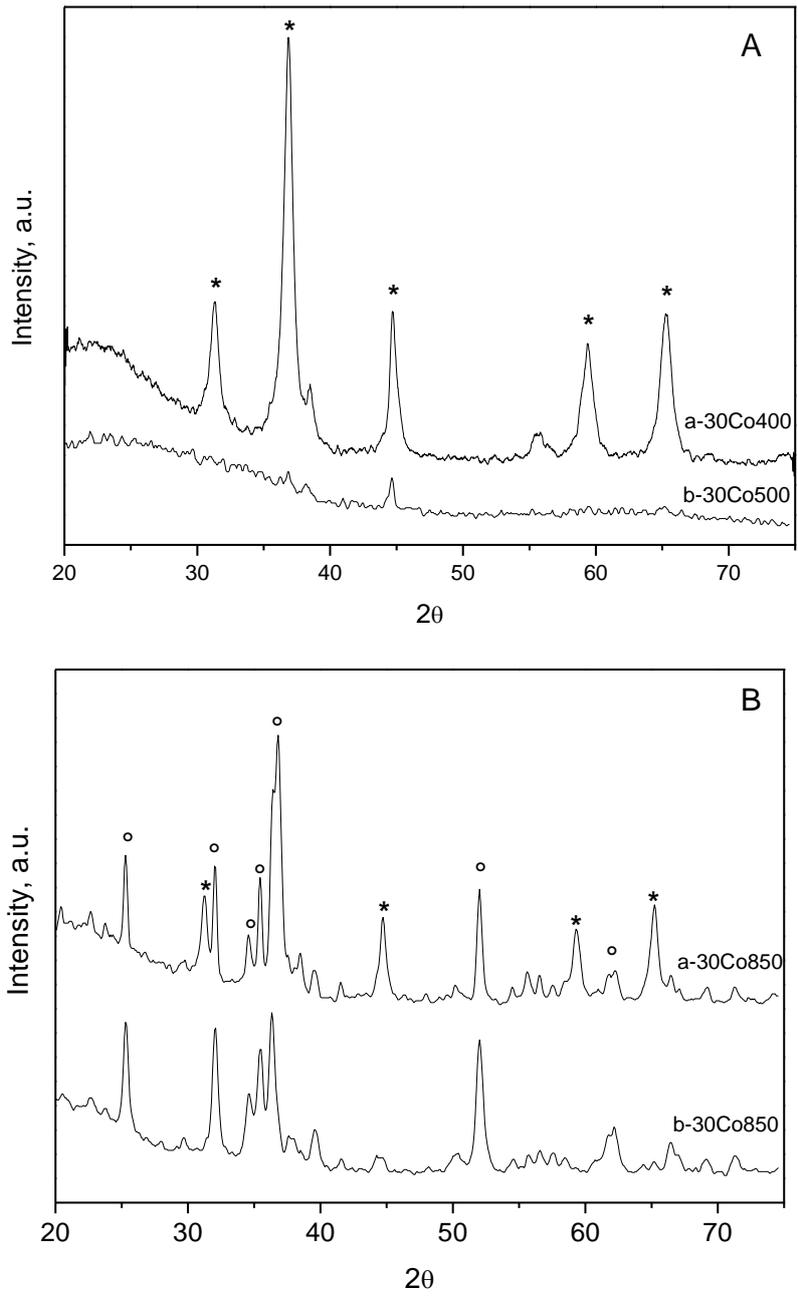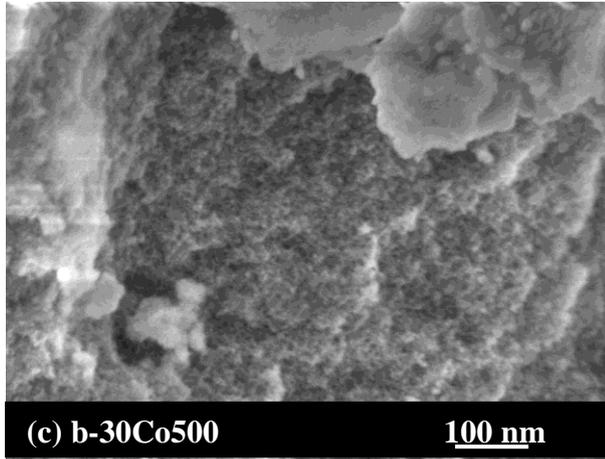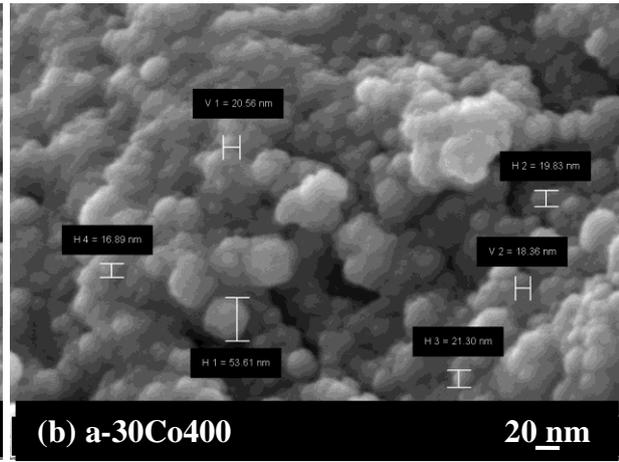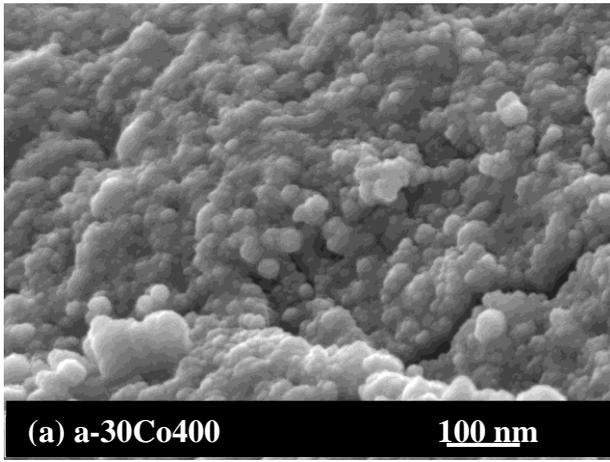
Fig. 3

Fig. 4

Fig. 5

Fig. 6

Fig. 7

Fig. 8